Corrosion Science 262 (2026) 113643

Contents lists available at ScienceDirect

Corrosion Science

journal homepage: www.elsevier.com/locate/corsci

Unraveling corrosion and tribocorrosion mechanisms of stainless steel in chloride/bromide media: The dual role of corrosion products

Yingpeng Zhang [a], Zheng Wang [b,c], Yalan Zhang [b,*], Lei Li [a], Peng Guo [b], Aiying Wang [b,d,**]

[a] School of Materials and Chemical Engineering, Ningbo University of Technology, Ningbo 315211, China
[b] State Key Laboratory of Advanced Marine Materials, Zhejiang Key Laboratory of Extreme-environmental Material Surfaces and Interfaces, Ningbo Institute of Materials Technology and Engineering, Chinese Academy of Sciences, Ningbo 315201, China
[c] Analytical Center, Ningbo Institute of Materials Technology and Engineering, Chinese Academy of Sciences, Ningbo 315201, China
[d] Center of Materials Science and Optoelectronics Engineering, University of Chinese Academy of Sciences, Beijing 100049, China

ARTICLE INFO

Keywords:
Stainless steel
Chloride ions
Bromide ions
Pitting corrosion
Tribocorrosion

ABSTRACT

Stainless steel components often face corrosion and tribocorrosion in various halide environments, as seen in applications like seawater plunger pumps, chemical agitators, and valves. Chloride (Cl^-) and bromide (Br^-) ions both degrade the corrosion and tribocorrosion resistance of stainless steel, yet their relative aggressiveness remains debated. Therefore, this study systematically compared the damage behavior of stainless steel in different halide environments using combined electrochemical and tribological techniques. Electrochemical corrosion analysis revealed Cl^- exhibited greater propensity than Br^- to displace oxygen within the Cr_2O_3 passive film and had a stronger penetration ability (smaller radius), rendering stainless steel more susceptible to pitting corrosion in Cl^- solutions. Resultant pits were larger, deeper, and more densely distributed. However, accumulated corrosion products such as Fe_xO_y inhibited Cl^- penetration, yielding a lower I_{corr} in Cl^- (3.58×10^{-9} A/cm^2) versus Br^- solutions (8.87×10^{-9} A/cm^2). Under tribocorrosion, copious Cl^--derived corrosion products acted as abrasive third bodies, exacerbating material loss versus Br^- environments, while wear-induced surface activation concurrently accelerated corrosion rates. This synergistic wear-corrosion interaction significantly elevated degradation, with corrosion-enhanced wear dominating material removal. Thus, while Cl^- more readily disrupted the Cr_2O_3 passive film, static corrosion products conferred protection via a "corrosion-product barrier" effect; under tribocorrosion, however, these protective oxides transformed into abrasive particles, amplifying degradation through mechano-electrochemical synergy.

1. Introduction

Stainless steels have become indispensable engineering materials across industrial equipment, architectural structures, and medical devices owing to their distinctive corrosion resistance, favorable mechanical strength, and exceptional hygienic properties [1–3]. However, localized corrosion of stainless steel is inevitable in environments rich in corrosive media (such as seawater, body fluids, chemical solutions, etc.). For instance, corrosion in high-salinity seawater environments poses severe threats to stainless steel, leading to structural damage in relevant components, reduced operational efficiency, and even potential issues such as hull failures that pose risks to human safety. Moreover, corrosion can also lead to severe consequences such as leakage in chemical pipelines, production shutdowns, and environmental pollution [4]. Therefore, understanding the corrosion behavior and failure mechanisms of stainless steel in various media is crucial, as it holds significant importance for preventing and mitigating accidents caused by corrosion.

Corrosion in solution is fundamentally an electrochemical issue. It is widely acknowledged that halogen elements (specifically Cl^- and Br^-) serve as primary initiators for the localized corrosion of stainless steel, due to the high susceptibility of the passive film to breakdown by these anions [5–12]. Interestingly, the relative impact of Cl^- versus Br^- on the corrosion of stainless steel remains a subject of ongoing debate. For example, Bardwell et al. investigated the relationship between Cl^-/Br^- and the pitting corrosion of iron, and their results demonstrated that at equivalent ionic concentrations, Cl^- exhibited greater aggressiveness

* Corresponding author.
** Corresponding author at: State Key Laboratory of Advanced Marine Materials, Zhejiang Key Laboratory of Extreme-environmental Material Surfaces and Interfaces, Ningbo Institute of Materials Technology and Engineering, Chinese Academy of Sciences, Ningbo 315201, China.
E-mail addresses: zhangyalan@nimte.ac.cn (Y. Zhang), aywang@nimte.ac.cn (A. Wang).

https://doi.org/10.1016/j.corsci.2026.113643
Received 18 September 2025; Received in revised form 14 December 2025; Accepted 19 January 2026
Available online 20 January 2026

towards the passive film than Br^- [9]. In contrast, Shao et al. conducted a comparative investigation into the corrosion behavior of stainless steel exposed to KCl, KBr, and their mixed solutions [10]. They claimed that Br^- had a higher equilibrium adsorption coefficient than Cl^-, and therefore was more corrosive to passive films. Furthermore, introducing Cl^- into Br^- solutions further enhanced its resistance to pitting corrosion. It is not difficult to see that Cl^- and Br^- in the solution are the main factors causing localized corrosion, but there is still controversy over which has a more significant impact. Furthermore, it is imperative to emphasize that stainless steel components are subjected not only to static corrosion but more critically, to a coupled tribocorrosion damage arising from the interplay of mechanical/tribological stresses and corrosive environments in dynamic systems (e.g., deep-sea drilling equipment, hydraulic transmissions, chemical valves). Typically, the synergy between wear and corrosion significantly compromises the structural stability and service lifespan of critical equipment [13–15]. Conversely, some studies have reported an antagonistic effect between wear and corrosion, which may, in some cases, unexpectedly prolong the service life of components [16,17]. Consequently, elucidating the tribocorrosion behavior of stainless steels across distinct halide environments represents an essential and urgent imperative. Regrettably, to the best of our knowledge, scarcely any comparative investigations into the tribocorrosion performance of stainless steels in Cl^- and Br^- solutions exist in the open literature.

Among many stainless steels, 17–4PH (a precipitation-hardening martensitic stainless steel) not only offers good corrosion resistance but also provides higher strength and hardness compared to materials like 304 and 316 L. Therefore, it is particularly suitable for key structural components that require high mechanical performance, such as those used in offshore platforms, seawater plunger pumps, and chemical valves [18–22]. In this work, employing 17–4PH stainless steel as a representative model, we systematically investigated its corrosion and tribocorrosion behaviors in Cl^-, Br^-, and mixed halide solutions. Through in-situ monitoring of corrosion and tribocorrosion processes under diverse electrochemical conditions, we aim to elucidate the influence of halogen elements (Cl^- and Br^-) on material degradation patterns and reveal the underlying damage mechanisms. It is anticipated that the findings will not only provide novel and comprehensive insights into the corrosion and tribocorrosion behavior of stainless steel in various halides but also offer valuable references for the protection of metallic materials (such as stainless steel) in corrosive environments.

2. Experimental details

2.1. Material preparation

A commercially available 17–4PH stainless steel (Fig. S1) was used in this study. Its chemical composition (wt% %) is as follows: 0.016 C, 0.43 Si, 0.45 Mn, 0.034 P, 0.001 S, 15.59 Cr, 3.92 Ni, 3.48 Cu, 0.19 Nb, balance Fe. Specimens in the form of cylindrical discs (3 mm × Φ17 mm) were sectioned using wire electrical discharge machining. Subsequently, the surfaces were progressively ground with SiC abrasive paper up to 3000 grit and polished to a mirror finish using a polishing cloth and diamond paste. Finally, the samples were ultrasonically cleaned in ethanol for 10 min, dried with lint-free cloths, and prepared for subsequent experimental testing.

2.2. Corrosion and tribocorrosion test

Electrochemical corrosion testing (ASTM G59–97) was conducted using an electrochemical workstation (ModuLab XM ECS) in 0.5 M KCl, 0.5 M KBr, and 0.25 M KCl + 0.25 M KBr solutions [23,24], with the corresponding samples designated as ClS, BrS, and ClBrS, respectively. A conventional three-electrode system was employed for all measurements: the stainless steel specimen served as the working electrode, a platinum plate as the counter electrode, and an Ag/AgCl electrode as the reference electrode. First, the open circuit potential (OCP) of each sample was continuously monitored for 10 h to observe its evolution. Subsequently, potentiodynamic polarization (PDP) tests were performed by scanning the potential from −0.5 V vs. OCP to + 1 V at a rate of 1 mV/s. After obtaining the polarization curves, Tafel plots were constructed with the potential on the y-axis and the logarithm of the current density on the x-axis. The Tafel extrapolation method was applied using the strong polarization region. The linear portions of both the cathodic and anodic branches were fitted to determine the Tafel slopes (β_c and β_a). These fitted lines were then extrapolated to intersect the horizontal line of the corrosion potential (E_{corr}). The current density at this intersection point is the corrosion current density (I_{corr}). Potentiostatic polarization (PSP) tests were conducted at a potential of + 0.1 V relative to the stable OCP. Additionally, electrochemical impedance spectroscopy (EIS) was performed before and after sliding under OCP conditions, with a frequency range of 10^5–10^{-2} Hz and an amplitude of 10 mV.

The tribocorrosion test was conducted using a tribometer (MFT5000, Rtec) coupled with an electrochemical workstation (Fig. 1). The tribometer operated in a reciprocating motion, with a Si_3N_4 ball (Φ6 mm) as the counter body under a normal load of 1 N ($\sigma_{max} \approx 717$ MPa) [25]. The sliding duration was 60 min, with a stroke length and speed set at 4 mm and 10 mm/s, respectively. The ambient temperature was 25°C, and all experiments were conducted in aqueous solution. Each tribological test was repeated three times to ensure the reliability of the results. To comparatively evaluate the tribocorrosion performance of stainless steel under distinct electrochemical conditions, tests were conducted under OCP, PDP, and PSP conditions, respectively. The electrochemical parameters were identical to those employed in the aforementioned corrosion tests. During all tribocorrosion tests, the coefficient of friction (COF), OCP, PDP, and PSP were monitored in situ and simultaneously by the tribometer and electrochemical workstation.

2.3. Characterization method

The morphology and elemental distribution of the samples were analyzed using a Quanta FEG 250 field emission scanning electron microscope (SEM, FEI, USA) equipped with an energy-dispersive X-ray spectroscopy (EDS) system. The three-dimensional images and topography of the wear tracks were examined using a 3D optical profiler (UP-Lambda, Rtec, USA), an Atomic Force Microscope (AFM, Bruker Dimension Icon, Germany), and a Zeiss optical microscope (Axio Imager 2). It should be noted that the cross-sectional area of the wear track, measured by 3D profilometry, is essential for determining the wear volume. Specifically, the wear rate (W) was calculated as follows [26]: $W = SL / FD$, where S is the cross-sectional area of the wear track, L is the wear track length, F is the normal load, and D is the total sliding distance. The Raman spectroscopy analysis was performed using a Horiba LabRAM HR Evolution system (Japan) with an excitation wavelength of 785 nm, covering a wavenumber range of 100 cm^{-1} to 3000 cm^{-1}. Samples were extracted using a focused ion beam (FIB, Zeiss, Germany), and the subsurface microstructure features of the wear tracks were observed using a TF20 scanning transmission electron microscope (STEM, FEI, USA). The concentrations of corrosion products in the solution were measured using inductively coupled plasma mass spectrometry (ICP-MS, Agilent 7800). Before testing, the solution was thoroughly shaken, and the precipitated species were digested using an acid dissolution method. The detailed instrument parameters were as follows: pump rate (20 r/min), nebulizer gas flow (1.00 L/min), auxiliary gas flow (1.00 L/min), sample flush time (40 s), and RF power (1550 W).

2.4. Theoretical computation

The spin-polarized Density Functional Theory (DFT) calculations were performed using the Cambridge Sequential Total Energy Package (CASTEP) module within Materials Studio [27–29]. The exchange

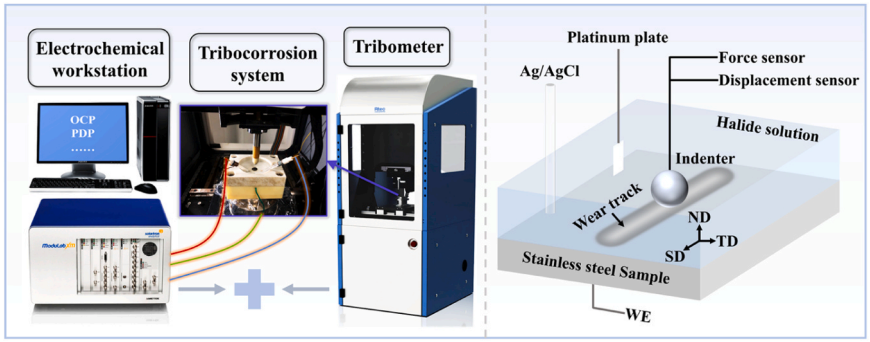

Fig. 1. Equipment and partial enlargement diagram for tribocorrosion testing, where SD, TD, and ND represent the sliding, transverse, and normal direction, respectively.

correlation function adopted the generalized gradient approximation of Perdew-Burke-Ernzerhof (PBE). The cutoff of kinetic energy was set to 450 eV, and the atomic positions were optimized until the Hellmann-Feynman force on each atom was less than 0.03 eV $Å^{-1}$. To improve efficiency, Brillouin zone sampling was tested and limited to a $3 \times 3 \times 1$ k-point mesh for structural optimization. To ensure the decoupling of the adjacent slabs, the 10 Å thick vacuum region along the surface was employed. The free energies of the reduction steps were calculated by the equation:

The adsorption energy (E_{ads}) is obtained by:

$$\triangle E_{ads} = E_{(ad+sub)} - E_{ad} - E_{sub} \quad (1)$$

The adsorption-free energy ($\triangle G_{ads}$) is obtained by:

$$\triangle G_{ads} = \triangle E_{ads} + \triangle ZPE - T\triangle S \quad (2)$$

where $\triangle ZPE$ and $\triangle S$ are the contributions to the free energy from the zero-point vibration energy and entropy, respectively.

3. Results and discussions

3.1. Electrochemical corrosion performance evaluation

The OCP-time curves of the ClS, ClBrS, and BrS samples are shown in Fig. 2a, with multiple tests conducted for each sample (two curves are presented). During the protracted 10 h measurement period, the OCP of ClS failed to attain a stable state, exhibiting substantial fluctuations. It is

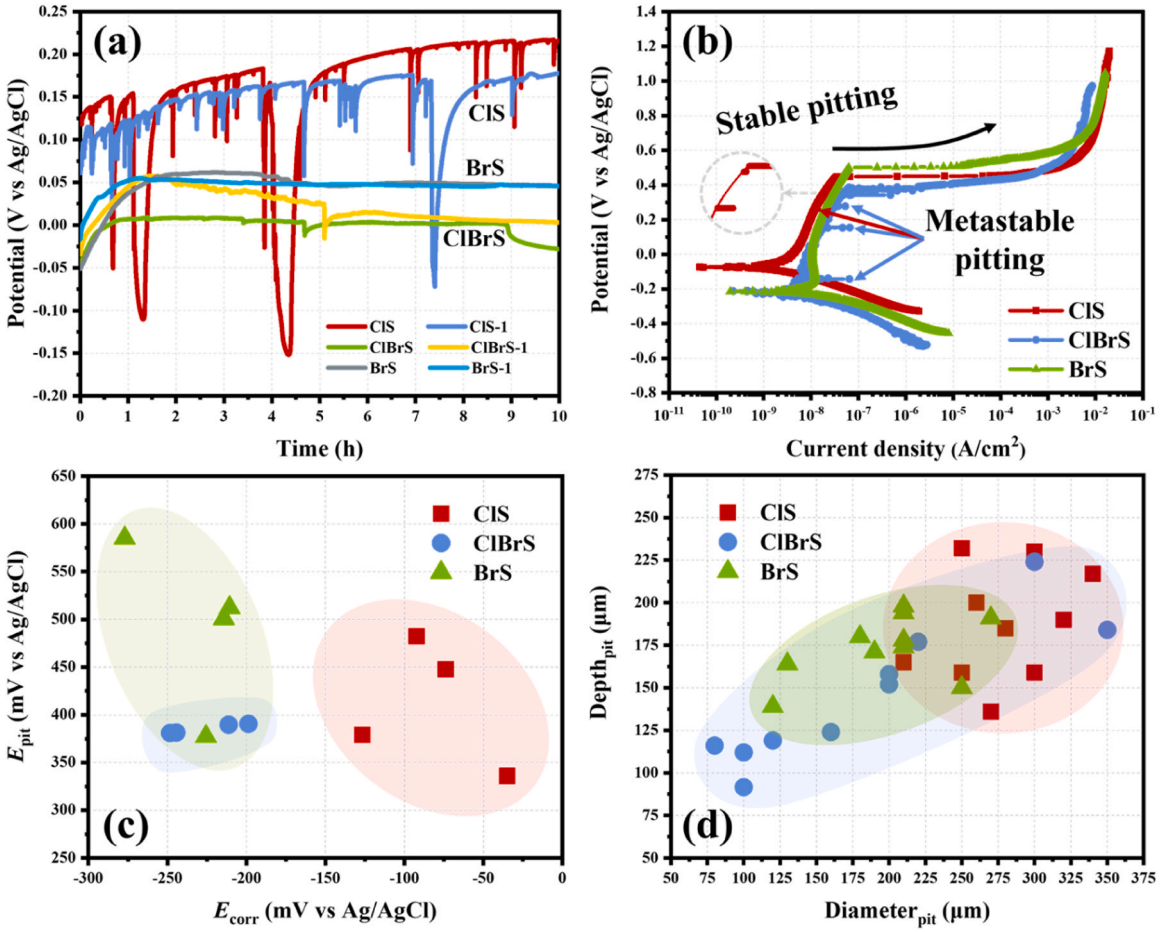

Fig. 2. (a) OCP, (b) PDP, (c) E_{pit}-E_{corr} and (d) $Depth_{pit}$-$Diameter_{pit}$ of ClS, ClBrS, and BrS.

speculated that the passive film of ClS will be severely damaged, exposing the highly electrochemically active metal substrate, which leads to a sudden potential drop. Subsequently, as the reaction proceeds, a new passive film will form, resulting in potential recovery. When Br^- ions were gradually introduced into ClS (ClS → ClBrS → BrS), the OCP progressively stabilized, but the potential values were relatively lower compared to ClS. This indicates that stainless steel undergoes more severe corrosion in Cl^- solution; however, the subsequent OCP is higher, demonstrating a phenomenon where corrosion inhibits corrosion. Following the OCP tests, the corrosion resistance of the ClS, ClBrS, and BrS samples was further evaluated by PDP tests. As presented in Fig. 2b, metastable pitting was observed in both ClS and ClBrS within the anodic passive region, while no such phenomenon was observed in BrS. This may be attributed to the greater tendency of Cl^-, compared to Br^-, to form soluble metal chlorides (e.g., $FeCl_2$, $CrCl_3$) with the passive film, thereby initiating metastable pitting. Moreover, the anodic Tafel slopes (β_a) for ClS, ClBrS, and BrS were 2006 mV/decade, 2194 mV/decade, and 2747 mV/decade, respectively. β_a reflects the difficulty of the anodic dissolution process. Generally, a higher slope indicates that the current density is less sensitive to changes in potential, meaning the process is more difficult to proceed, which suggests greater stability of the passive film [30]. Therefore, this also indicates that the passive film of stainless steel is more stable in Br^- solution than in Cl^- solution, which is consistent with the OCP results.

The steady-state pitting potential (E_{pit}) and self-corrosion potential (E_{corr}) of the three samples are presented in Fig. 2c (statistical results from multiple measurements). The observed variation in these values for the stainless steel in the same solution is likely attributable to the inherent surface heterogeneity of the material. Firstly, minor differences inevitably arise during grinding and polishing, which can lead to slight variations in surface roughness, residual stress, and the thickness of the deformed layer, consequently affecting the uniformity and protective quality of the passive film. Secondly, inclusions serve as the most susceptible initiation sites for pitting. The number, size, and distribution of inclusions can differ slightly from one sample to another. Even at different locations on the same sample, the exposed sensitive sites after polishing can vary, leading to differences in the measured pitting potential. In summary, the variation in pitting and corrosion potentials for the same stainless steel in the same solution is a normal phenomenon, primarily caused by this surface heterogeneity. Recognizing its statistical nature, we conducted standardized, repeated experiments to minimize random error and obtain reliable, comparable key data. The results indicated that the average E_{pit} of BrS (493.93 ± 86.29 mV) was higher than that of ClBrS (385.68 ± 5.18 mV) and ClS (411.35 ± 66.09 mV), demonstrating enhanced pitting resistance of the stainless steel in the Br^- solution. Intriguingly, however, the average E_{corr} of ClS (-81.92 ± 38.20 mV) was significantly higher than that of ClBrS (-225.63 ± 24.46 mV) and BrS (-231.85 ± 30.77 mV). Generally, a higher E_{corr} implies a lower corrosion tendency [31], suggesting that ClS exhibits a lower corrosion tendency compared to ClBrS and BrS. Moreover, Tafel extrapolation revealed that the average corrosion current density (I_{corr}) of ClS (3.58×10^{-9} A/cm^2) was also lower than that of ClBrS (5.53×10^{-9} A/cm^2) and BrS (8.87×10^{-9} A/cm^2), confirming the lowest corrosion rate of the stainless steel in the Cl^- solution. It can be inferred that stainless steel is more susceptible to corrosion initiation in Cl^- solutions, yet exhibits a lower corrosion rate compared to Br^- solutions. This observation is consistent with the findings from the OCP measurements. It is postulated that while Cl^- exhibits stronger aggressiveness towards the passive film, leading to more severe localized attack, the subsequent accumulation of corrosion products hinders further corrosion propagation. Shao et al. also reported a lower I_{corr} for stainless steel in Cl^- solutions compared to Br^- solutions and attributed this phenomenon unexpectedly to a protective role of Cl^- ions in the corrosion process of stainless steel [10].

The post-PDP morphologies of the three samples are presented in Fig. S2 (Supporting Information). It was observed that ClS exhibited large and dense corrosion pits, indicating severe pitting damage. As Br^- was introduced and the Cl^- content decreased, the pit size progressively diminished, accompanied by a reduction in pit density. After each PDP test, 10 corrosion pits were measured in descending order of size using a 3D optical profiler. This PDP test was repeated four times, resulting in a cumulative total of 40 pit dimension measurements. As shown in Fig. 2d, 10 representative pits are displayed for each sample, with the size of each pit being the average of four independent measurements. The depth and diameter of the corrosion pits were statistically analyzed. Overall, the average pit depth and diameter of ClS (187 μm, 278 μm) were larger than those of BrS (174 μm, 198 μm), while ClBrS exhibited an intermediate size range with significant dispersion. Before characterizing the pits, it was intentional to leave the corrosion products of the stainless steel in the solution. Consequently, it can be inferred from the exposed substrate that ClS sustained substantially more severe corrosion damage than BrS. This experimental evidence confirms that Cl^-, rather than Br^-, acts as the primary aggressive species responsible for stainless steel corrosion.

3.2. Analysis of corrosion mechanisms

To further investigate the corrosion behavior of ClS, ClBrS, and BrS, the solutions after PDP tests were collected (Fig. 3a) and subjected to quantitative analysis of the corrosion products within them (Fig. 3b). For each PDP test, the electrolyte volume was maintained at 300 mL. Post-test, the solution was vigorously agitated to ensure complete transfer of precipitated corrosion products from the stainless steel surface into the solution, thereby guaranteeing the reliability of subsequent quantitative analyses. As evidenced in Fig. 3a, the ClS solution exhibited the darkest, rust-colored hue, indicative of severe corrosion. With decreasing Cl^- and increasing Br^- content, the solution color progressively lightened to near-colorless (BrS). This visual gradient provides compelling evidence that stainless steel undergoes more severe corrosion in Cl^- solutions compared to Br^-. Furthermore, upon prolonged standing, substantial rusty-brown precipitates formed in the ClS solution, while ClBrS developed yellow deposits. In contrast, only scant traces of pale-yellow deposition were observed in the BrS solution. This observation indicates that corrosion in ClS was more exhaustive, resulting in more substantial accumulation of corrosion products. The voluminous deposition impedes the diffusion of aggressive ions toward the stainless steel interior, thereby suppressing ongoing corrosion. This provides a coherent explanation for the OCP and PDP results: Firstly, elevated Cl^- content intensifies OCP fluctuations yet elevates the potential value. Secondly, compared to BrS, ClS demonstrates a higher E_{corr} and lower I_{corr} but exhibits more pronounced pitting damage. These findings corroborate the postulated “corrosion inhibits corrosion” mechanism introduced earlier.

To quantitatively evaluate the corrosion extent of ClS, ClBrS, and BrS samples, the metal ion contents (Fe and Cr) in post-corrosion solutions were analytically determined. Quantitative analysis revealed Fe concentrations of 48.10 mg/L in ClS, exceeding ClBrS and BrS by 68 % and 72 %, respectively. Similarly, Cr content in ClS (1.70 mg/L) substantially surpassed levels in ClBrS (1.49 mg/L) and BrS (0.72 mg/L). These findings demonstrate that Cl^- exhibits more pronounced aggressiveness toward the passive film than Br^-, consequently inducing more severe stainless steel corrosion, evidenced by elevated metal dissolution products.

The passive film on stainless steel typically has a layered structure: an outer layer rich in iron oxides/hydroxides covers an inner layer primarily made of Cr_2O_3 [32,33]. While the outer layer is characteristically porous, the inner layer is densely compacted. This dense inner layer is the key factor responsible for stainless steel’s superior corrosion resistance. Currently, there are two main models for the mechanism of passive film destruction induced by halide ions such as Cl^- and Br^-: the displacement model and the penetration model [6,34–37]. Regarding the displacement model, the corrosion thermodynamics of Cr_2O_3 in

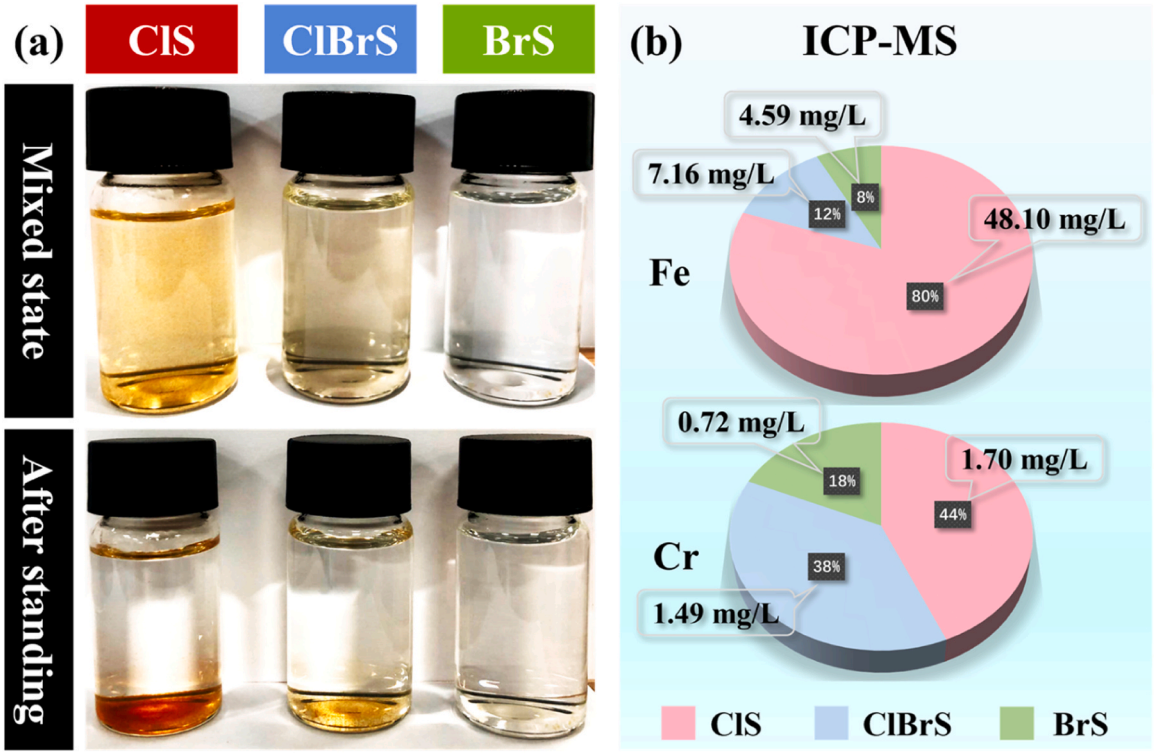

Fig. 3. Corrosion solution analysis of ClS, ClBrS, and BrS after PDP testing: (a) macroscopic morphology, (b) ICP-MS results.

halides were studied using DFT (Fig. 4a). The results indicated that Cr_2O_3_ov to the intermediate product Cr_2O_3ov_Cl (-2.35 eV, Cr_2O_3 with oxygen displaced by halide) had lower free energy compared to Cr_2O_3ov_Br (-1.10 eV). More importantly, in the rate-determining step (RDS, Cr-Cl/Br detachment from the Cr_2O_3ov_Cl/Br intermediate product), the RDS free energy of ClS (0.16 eV) was much lower than that of BrS (1.42 eV), indicating that Cr_2O_3 was more susceptible to Cl^- corrosion, which was consistent with the PDP results. Furthermore, regarding the penetration model (Fig. 4b), the radius of Cl^- (0.181 nm) is smaller than that of Br^- (0.196 nm), indicating that Cl^- has a stronger penetration ability than Br^- and is therefore more likely to destroy the Cr_2O_3 passive film. The above results indicate that compared with Br^-, Cl^- is more likely to displace oxygen in the Cr_2O_3 passive film and has a stronger ability to penetrate the passive film. Combining experimental and theoretical calculation results, the corrosion process of ClS, ClBrS, and BrS samples can be explained as follows. The passive film on the stainless steel surface is more susceptible to attack by Cl^-, leading to severe pitting corrosion with large and dense pits. As the corrosion process progresses, corrosion products gradually accumulate (Fe_xO_y and Cr_2O_3). At this point, the corrosion rate of ClS decreases significantly, even falling below that of ClBrS and BrS. In short, in a static environment, Cl^- is more aggressive than Br^- in attacking the passive film of stainless steel, but the subsequent accumulation of numerous corrosion products in turn inhibits further corrosion.

3.3. Tribocorrosion behavior under various electrochemical conditions

As established in preceding analyses, stainless steel exhibits heightened susceptibility to pitting corrosion in static Cl^--containing environments, resulting in accelerated accumulation of corrosion products. Subsequently, the sliding behavior of stainless steel under various electrochemical conditions (OCP, PDP, PSP) will be investigated to evaluate its dynamic tribocorrosion performance in Cl^- and Br^- solutions in detail.

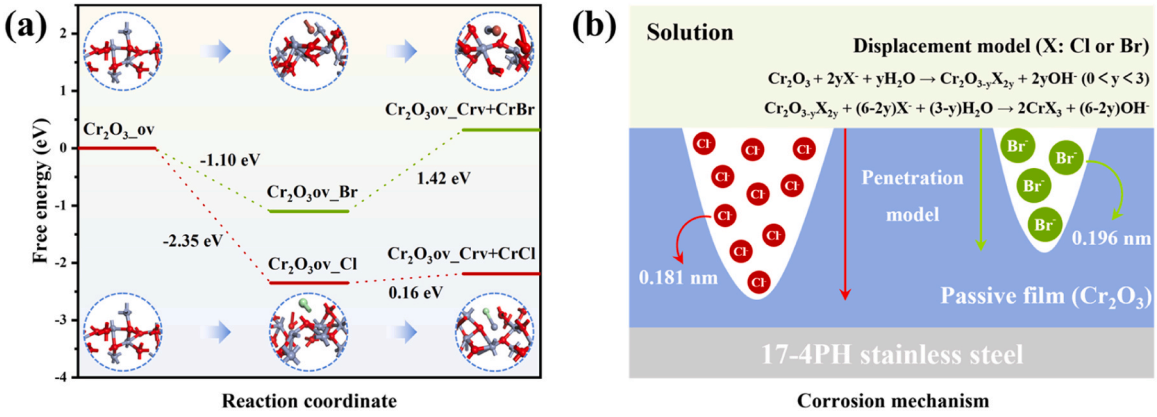

Fig. 4. (a) Calculated free-energy diagrams for Cr_2O_3 corroded by halide, where ov denotes the oxygen vacancy and Crv denotes the Cr vacancy, (b) schematic diagram of the mechanism of Cr_2O_3 passive film destruction.

3.3.1. Tribocorrosion behavior under OCP conditions

The tribocorrosion results of ClS, ClBrS, and BrS under OCP conditions are shown in Fig. 5. In Fig. 5a, it was found that the COF of the three samples was comparable, all stable between 0.40 and 0.45, indicating that the effect of different halides on the COF of stainless steel under OCP conditions is limited. Under OCP conditions, the stainless steel samples were in a state of natural corrosion with a relatively slow corrosion rate. Thus, during sliding under OCP, although the corrosion rates of the samples differed slightly, they were almost in a state of pure friction (with negligible influence from corrosion), leading to nearly identical COF values for all samples. Fig. 5b shows the changes in OCP values during the tribocorrosion process. At the start of sliding, the OCP values of all samples dropped sharply, then entered a plateau phase with slight fluctuations during the sliding process. After sliding, the OCP of all samples quickly rebounded until it reached a stable level. According to the Mixed Potential Theory (MPT), during sliding contact, only specific regions of stainless steel experience mechanical loading effects [31,38]. Consequently, the measured overall potential constitutes a mixed potential originating from the depassivated zone within the wear track and the passivated regions outside. Upon initiation of sliding, localized removal of passive films occurs on stainless steel surfaces. This accounts for the instantaneous potential drop observed in ClS, ClBrS, and BrS samples. During sliding, a dynamic equilibrium between depassivation and repassivation processes is maintained within the wear track, resulting in a stabilized potential plateau accompanied by minor fluctuations. Notably, the average potential drop ($E_{initial}$ - $E_{plateau}$) for ClS (↓0.423 V) exceeded that of ClBrS (↓0.387 V) and BrS (↓0.353 V). Based on MPT, we preliminarily infer that sliding in Cl^- solutions exposes a larger nascent metal surface area, thereby inducing a greater potential drop, reflecting significantly enhanced corrosion tendency. This mechanism will be elucidated in subsequent sections.

The repassivation rate after sliding can be determined using the following equation [39]:

$$\Delta E = k_1 \log t + k_2 \quad (3)$$

where ΔE is the potential shift, t is the time after sliding cessation, k_1 represents the repassivation rate, and k_2 is a solution-dependent constant. The calculated results indicated that ClS exhibited a significantly larger k_1 value (0.123) compared to ClBrS (0.07) and BrS (0.053), implying superior repassivation capability after sliding. Furthermore, the EIS of ClS after sliding showed the closest alignment with that before sliding (Fig. S3), with its $|Z|_{0.01\ Hz}$ value recovery rate reaching 76.3 %, significantly higher than those of ClBrS (54.6 %) and BrS (51.4 %). This further demonstrates that ClS possesses a stronger repassivation ability compared to the other samples. As noted previously, Cl^- exhibits stronger aggressiveness than Br^- toward Cr_2O_3, leading to enhanced formation of corrosion products (Fe_xO_y and Cr_2O_3). This accounts for the faster and higher potential recovery observed in ClS after sliding compared to ClBrS and BrS. Fig. 5c shows the cross-sectional areas of the wear tracks for the three samples. Compared with ClBrS (205 μm^2) and BrS (181 μm^2), ClS (258 μm^2) exhibited the largest cross-sectional area. Furthermore, the 3D topographic profiles (Fig. 5d) reveal that the wear tracks of all samples are composed of accumulated wear debris and relatively deep grooves.

The wear tracks of ClS, ClBrS, and BrS after sliding under OCP conditions were further characterized using OM and SEM-EDS techniques. From the OM images (Fig. 6a, b, c), the wear track width of ClS (329 μm) was observed to be greater than that of ClBrS (321 μm) and BrS (290 μm), suggesting that the ClS sample experienced more severe wear compared to ClBrS and BrS. This provides a reasonable explanation for the observation that ClS exhibited the largest potential drop during sliding (Fig. 5b). The interiors of the wear tracks for all samples (Fig. 6d, e, f) were distributed with ridge-like band-shaped oxides and numerous grooves. During sliding, the wear tracks consisted of fresh metallic substrate and passive films formed by repassivation. The metallic substrate, having relatively low hardness, is prone to adhering to the wear track and counterbody surfaces due to cold welding during sliding, thereby inducing adhesive wear. In contrast, the passive films exhibit relatively high hardness and can act as hard third bodies during sliding, leading to severe abrasive wear. Consequently, it can be concluded that the wear mechanisms for all samples sliding under OCP conditions comprise both adhesive wear and abrasive wear.

Liu et al. point out that the abrasive wear induced by the passive film on stainless steel is the primary cause of material loss [40]. Static corrosion tests revealed that the ClS sample exhibited more severe

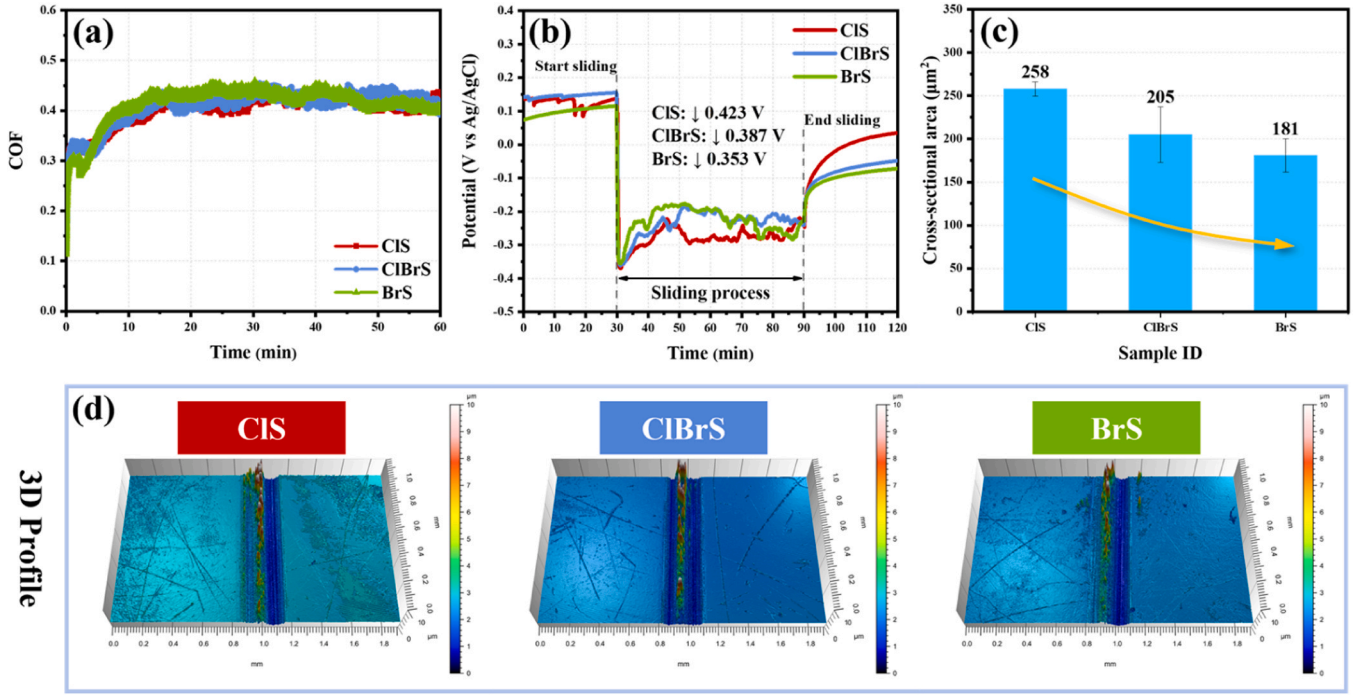

Fig. 5. Tribocorrosion results of ClS, ClBrS, and BrS under OCP conditions: (a) COF, (b) OCP, (c, d) cross-sectional area and 3D profile of wear tracks.

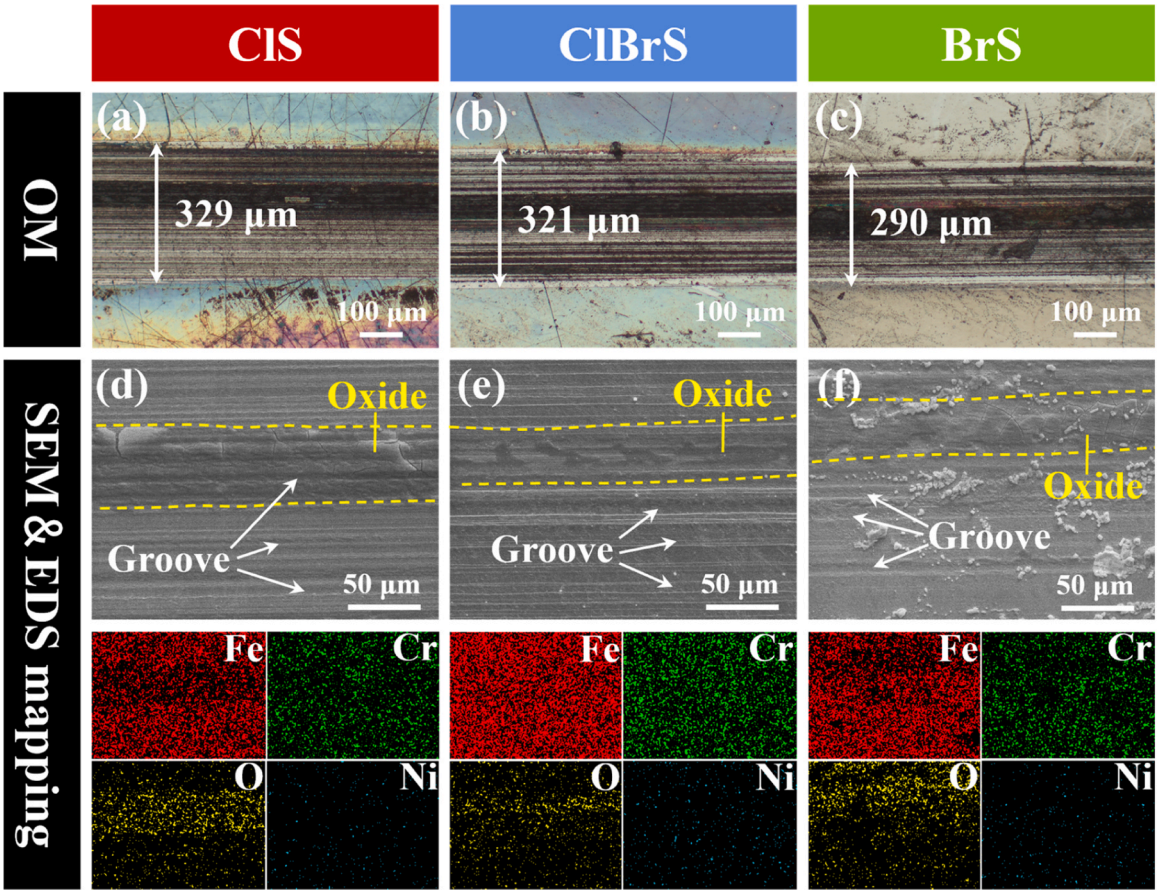

Fig. 6. Morphology and elemental distribution of wear tracks after sliding under OCP conditions for (a, d) ClS, (b, e) ClBrS, and (c, f) BrS.

corrosion and a greater amount of metal oxides (passive films) compared to the ClBrS and BrS samples. Consequently, during sliding, ClS is expected to undergo more severe abrasive wear, leading to accelerated material loss. By contrast, the BrS sample surface possessed fewer oxides. Therefore, the material loss induced by sliding was the lowest for BrS (Fig. 5c), its wear track width was the narrowest (Fig. 6c), and it

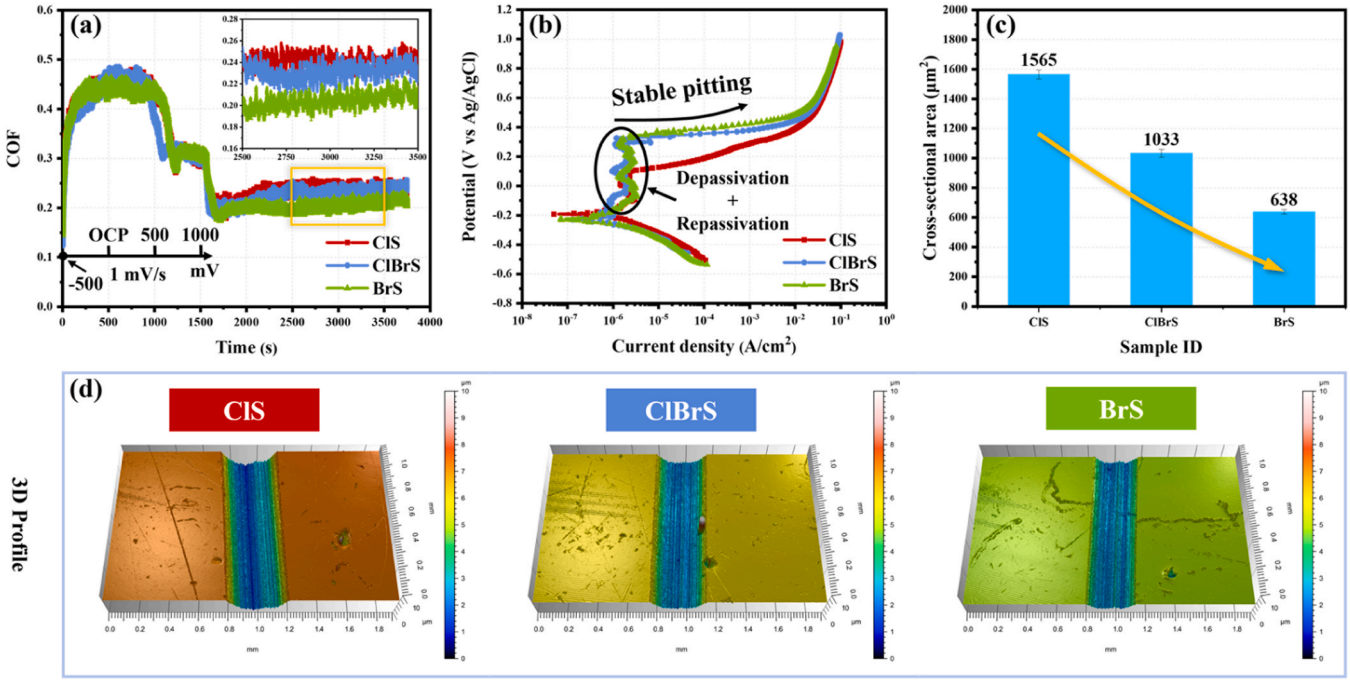

Fig. 7. Tribocorrosion results of ClS, ClBrS, and BrS under PDP conditions: (a) COF, (b) PDP, (c, d) cross-sectional area and 3D profile of wear tracks.

exhibited the smallest potential drop (Fig. 5b). In short, the ClS sample with high Cl^- content is more prone to pitting corrosion, resulting in the formation of a greater amount of oxide passive films. These passive films induce more severe abrasive wear, accelerating material loss. Furthermore, the wider and deeper wear track exposes more fresh metallic surfaces, which further intensifies corrosive damage, forming a self-accelerating "corrosion → wear → re-corrosion" chain reaction.

3.3.2. Tribocorrosion behavior under PDP conditions

Fig. 7 presents the tribocorrosion results for ClS, ClBrS, and BrS samples under PDP conditions. Within the potential range of −500 mV to OCP (Fig. 7a), the COF values for all three samples were high, reaching ~0.45. When the potential was within the range of OCP to 500 mV, the COF for all samples continuously decreased to ~0.3. As the potential increased to 1000 mV, the COF dropped sharply to ~0.2. As previously described (Fig. 6), during sliding at and below OCP, the wear manifested as a mixed mode dominated by adhesive wear combined with abrasive wear, corresponding to the very high COF observed for all samples. It can therefore be deduced that when the potential is raised above OCP, anodic polarization promotes the formation of passive films (metal oxides), rendering the wear track surface harder and smoother. Consequently, the wear mechanism gradually transitions from being adhesive-dominant to abrasive-dominant, leading to the continuous decrease in COF. As the potential increases beyond 500 mV, the wear track becomes predominantly covered with hard passive films, preventing the counterbody from contacting the softer metallic substrate. Under these conditions, adhesive wear ceases, and the wear mechanism for all samples shifts to purely abrasive wear, resulting in the lowest COF (~0.2). Interestingly, when the potential dropped back, the COF of all samples showed no rebound. This phenomenon is likely attributable to the substantial hard passive film on the counterbody, which prevented subsequent adhesive wear, thereby maintaining a consistently low COF. As evidenced in the inset of Fig. 7a, the COF of ClS (~0.24) was marginally higher than those of ClBrS (~0.22) and BrS (~0.20). This discrepancy stems from Cl^- promoting passive film regeneration, consequently intensifying abrasive wear.

Fig. 7b presents the PDP curves of ClS, ClBrS, and BrS under sliding. In the anodic passive region, all specimens exhibited combined depassivation-repassivation behavior, resulting from periodic removal of passive films by mechanical sliding. Notably, the steady-state pitting potential of ClS (0.11 V) was significantly lower than those of ClBrS (0.32 V) and BrS (0.34 V), indicating markedly enhanced susceptibility to pitting corrosion under sliding conditions. Unlike in static conditions (Fig. 2b), the I_{corr} of ClS (9.73×10^{-7} A/cm^2) was significantly higher than that of ClBrS (6.42×10^{-7} A/cm^2) and BrS (4.61×10^{-7} A/cm^2) under sliding. This acceleration effect stems from mechanical sliding, preventing the accumulation of corrosion products, thereby eliminating their auto-inhibiting function. Consequently, stainless steel experiences enhanced corrosion rates in highly aggressive Cl^- solutions, as reflected by the elevated I_{corr} values.

As revealed in Fig. 7(c, d), the cross-sectional area of wear tracks reached 1565 μm^2 for ClS under PDP conditions, significantly surpassing those of ClBrS (1033 μm^2) and BrS (638 μm^2). Further analysis was performed on the wear track morphologies of ClS, ClBrS, and BrS after sliding under PDP conditions (Fig. S4). The results revealed that the wear track width of ClS reached 413 μm, which was significantly wider than those of ClBrS (376 μm) and BrS (327 μm). Moreover, band-shaped oxides, which were observed after sliding under OCP conditions, were not found in the wear tracks of any samples. Instead, only a large number of grooves and a small amount of abrasive particles were observed. This phenomenon indicates that during sliding under PDP conditions, the dominant wear mechanism transitions from adhesive wear to abrasive wear as the potential increases. Furthermore, even after the potential reverses, adhesive wear does not readily revert. This observation supports the previous hypothesis regarding the change in COF (Fig. 7a). Notably, ClS experienced more severe abrasive wear compared to ClBrS and BrS. This behavior is consistent with that observed during sliding under OCP conditions and is similarly attributed to the accelerated formation of metal oxides promoted by Cl^- ions, which consequently exacerbates abrasive wear. Interestingly, no metastable pitting occurred during sliding in any of the samples. Moreover, although the electrochemical data in Fig. 7b suggest the occurrence of stable pitting, no pits like those in static PDP tests were found in the micrograph in Fig. 7d. This is because the region where the passive film was removed by friction can be regarded as a "weak zone" of the entire sample. Compared to the non-sliding area, this weak zone has much higher electrochemical activity. Therefore, the entire wear track can be considered equivalent to one large corrosion pit. Even when the wear track undergoes self-healing (repassivation), new weak zones are continuously regenerated by the reciprocating sliding. Fig. S5 provides a clearer illustration of this process. Both ClS and BrS exhibited numerous corrosion pits after static corrosion tests. However, during dynamic tribocorrosion, both metastable and stable pitting phenomena are masked by the strong effect of mechanical removal of the passive film caused by sliding. Consequently, the corrosion pits disappeared and were replaced by wear tracks covered with plowing grooves and abrasive particles. It is worth noting that pitting was much more severe on ClS than on BrS, resulting in a larger amount of corrosion products that led to more significant abrasive wear. This synergistic effect between corrosion and wear further enhanced the tribocorrosion damage of the stainless steel.

3.3.3. Tribocorrosion behavior under PSP conditions

In addition to the OCP and PDP conditions, sliding tests were also conducted on the ClS, ClBrS, and BrS samples under PSP conditions (100 mV vs. OCP) to investigate their tribocorrosion behavior under a sustained passive potential. As shown in Fig. 8a, the COF values for all samples remained below 0.4, stabilizing between 0.3 and 0.35 under the passive potential sliding condition. This low and stable COF suggests that abrasive wear was the dominant wear mechanism for these samples. Furthermore, the COF of ClS (~0.35) and ClBrS (~0.35) was slightly higher than that of BrS (~0.31). This difference is likely due to the accelerated generation of corrosion products promoted by the aggressive Cl^- ions, thereby inducing more severe abrasive wear in ClS and ClBrS. As shown in Fig. 8b, the average current density of ClS during sliding reached 1.07×10^{-4} A/cm^2, which was significantly higher than those of ClBrS (7.67×10^{-5} A/cm^2) and BrS (6.23×10^{-5} A/cm^2). This indicates that ClS exhibited the largest exposure of fresh active surfaces among the samples. It is also noted that the current densities before and after sliding showed no significant difference for all three samples, suggesting that the observed differences primarily originated from the dynamic wear process. As observed in Fig. 8(c, d), the wear tracks on all three samples were wide and deep. Notably, the cross-sectional area of the wear track on ClS reached 4191 μm^2, which was significantly larger than that on ClBrS (3094 μm^2) and BrS (2736 μm^2). This trend is consistent with the observations made during sliding under both OCP and PDP conditions, as previously discussed. Critically, the material loss of all three samples during sliding under PSP conditions far exceeded that observed under both OCP and PDP conditions. This demonstrates that the wear of stainless steel was most severe under the sustained passive potential and least severe under natural conditions (OCP). This finding provides compelling evidence supporting the hypothesis that passive films/metal oxides significantly exacerbate wear damage.

Furthermore, after sliding under PSP conditions, the wear track widths of ClS, ClBrS, and BrS reached 562 μm, 511 μm, and 494 μm, respectively, exhibiting a monotonically decreasing trend (Fig. S6). Moreover, examination of the wear tracks on all three samples revealed a large number of grooves and abrasive particles (Fig. 8e), indicating that severe abrasive wear, caused by the hard passive film, was the dominant wear mechanism. As discussed previously, Cl^- ions are more aggressive towards Cr_2O_3, generating a greater amount of corrosion products (metal oxides), which subsequently resulted in more severe

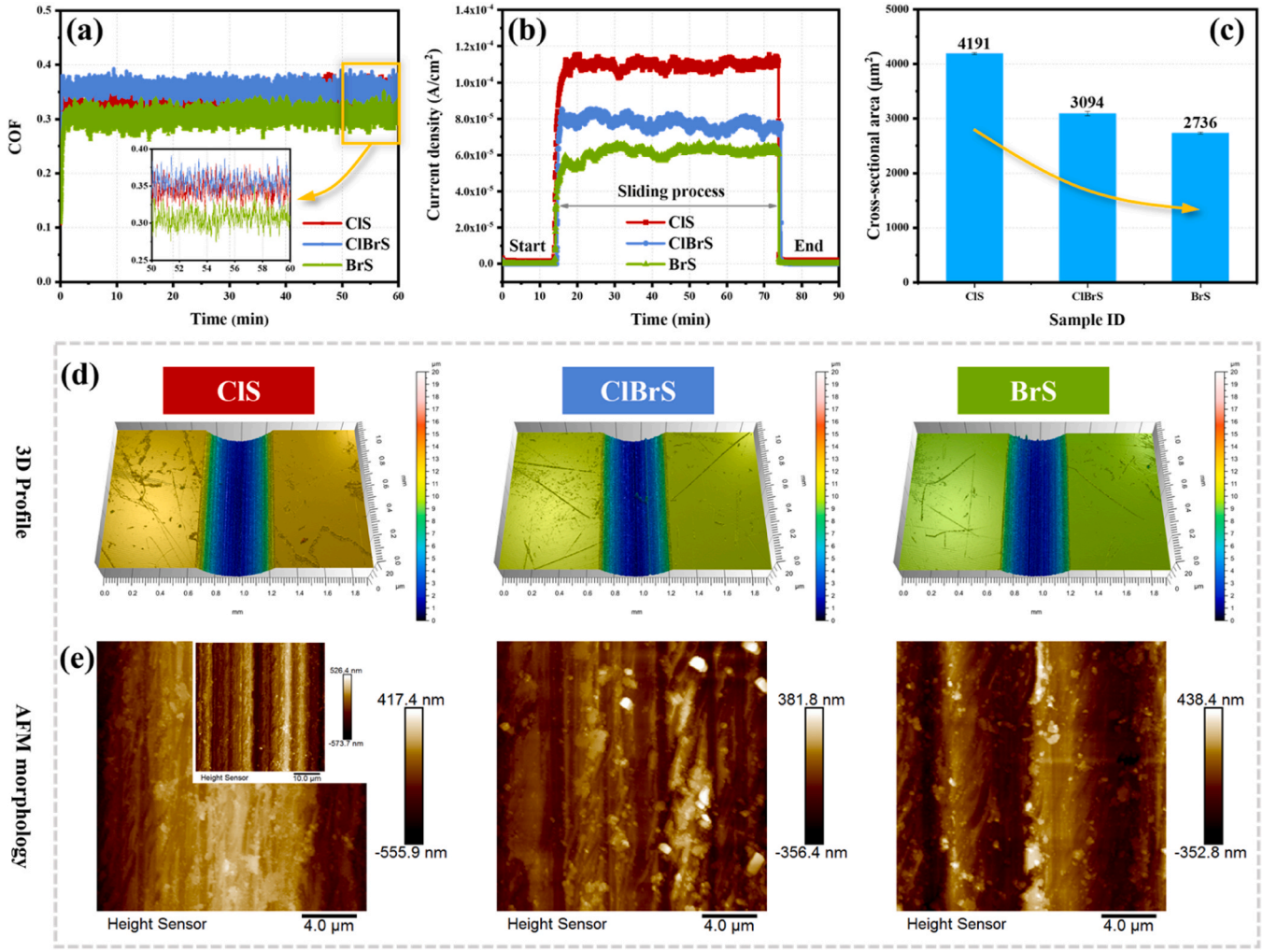

Fig. 8. Tribocorrosion results of ClS, ClBrS, and BrS under PSP conditions: (a) COF, (b) current density, (c) cross-sectional area, (d) 3D profile, and (e) AFM morphology of the wear tracks.

abrasive wear.

To gain deeper insights into the characteristics of the passive films on ClS and BrS samples after sliding under PSP conditions, detailed characterization was performed using FIB-STEM technology. As shown in Fig. 9a, a FIB sample was extracted and thinned perpendicular to the sliding direction on the ClS. This revealed that the sample was predominantly covered by a continuous chromium oxide layer. Further analysis using HRTEM and FFT (Fig. 9b) demonstrated that this chromium oxide layer was approximately 4–5 nm thick and existed in an amorphous state. Interestingly, a similar amorphous chromium oxide layer was observed on the BrS samples (Fig. 9c, d). This implies that the characteristics of the Cr_2O_3 passive films on ClS and BrS showed no significant differences. Additionally, the chemical composition of the passive film on ClS and BrS surfaces was analyzed by XPS spectroscopy (Fig. S7), including the Fe 2p and Cr 2p spectra. For the ClS sample, the Fe 2p spectrum was fitted into Fe^0 and Fe^{III}-O (Fe $2p_{3/2}$, Fe $2p_{1/2}$) peaks with binding energies of 706.5 eV, 710.8 eV, and 724.5 eV, respectively. The Cr 2p spectrum was fitted into Cr^{III}-O (Cr $2p_{3/2}$, Cr $2p_{1/2}$) peaks with binding energies of 576.8 eV and 586.5 eV [41,42]. For the BrS sample, the Fe 2p spectrum was fitted into Fe^{III}-O (Fe $2p_{3/2}$, Fe $2p_{1/2}$) peaks, and the Cr 2p spectrum was fitted into Cr^{III}-O (Cr $2p_{3/2}$, Cr $2p_{1/2}$) peaks.

It can be observed that the passive film surface mainly consists of iron oxide and chromium oxide. Extensive research confirms that the passive film of stainless steel has a dual-layer structure: a porous Fe-rich outer oxide (Fe_xO_y) and a dense, adherent Cr_2O_3 inner layer serving as the main corrosion barrier [32,33,43–46]. It is noteworthy that Fe^0 was detected in ClS but not in BrS. Metallic Fe is typically present in the stainless steel substrate beneath the passive film. This suggests that the passive film on ClS may contain more defects or be thinner compared to that on BrS [41,47]. Notably, under PSP sliding conditions (Fig. 8), the wear rate of ClS (4.66×10^{-4} $mm^3/N{\cdot}m$) was significantly higher than that of ClBrS (3.44×10^{-4} $mm^3/N{\cdot}m$) and BrS (3.04×10^{-4} $mm^3/N{\cdot}m$). This phenomenon can be interpreted from two perspectives. First, as previously discussed, ClS exhibited a substantially higher repassivation rate (0.123) compared to ClBrS (0.07) and BrS (0.053), resulting in more severe abrasive wear. Second, the intensified abrasive wear led to greater exposure of the active surface on ClS (manifested as higher current density), thereby further contributing to accelerated material loss.

3.4. Synergistic interaction of tribocorrosion

Tribocorrosion testing of stainless steel in halide-containing solutions reveals that corrosion and wear processes synergistically accelerate material degradation. This interaction results in a total volume loss exceeding the arithmetic sum of individual corrosion and wear losses. Quantifying the dynamic interplay between corrosion and wear during sliding would undoubtedly advance fundamental understanding of stainless steel tribocorrosion mechanisms. Therefore, to quantitatively determine the tribocorrosion synergy in ClS, ClBrS, and BrS, the pro-

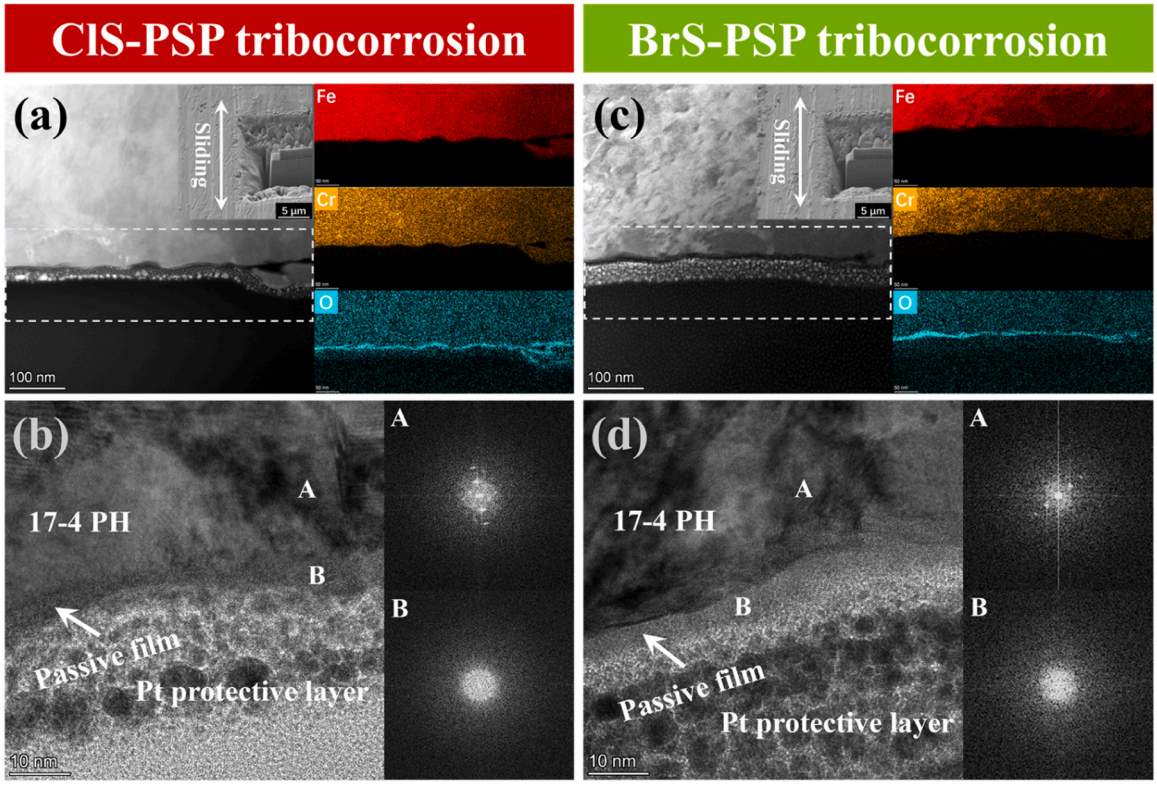

Fig. 9. The cross-sectional SEM, EDS mapping, HRTEM, and FFT images of the wear tracks for (a, b) ClS and (c, d) BrS after PSP tribocorrosion.

portional contributions to total volume loss during sliding were calculated using the following equations [48]:

$$V_t = V_f + V_c + V_{f-c} + V_{c-f} \tag{4}$$

where V_t is the total volume loss under polarization, V_f and V_c represent the pure friction and pure corrosion volume losses, respectively. It should be noted that the oxidation/corrosion rate under OCP conditions was much lower than under PDP and PSP conditions, allowing it to be approximated as a pure friction process. Thus, the volume loss measured under OCP conditions was used as V_f in this study. V_c is determined by:

$$V_c = \frac{I_c * M * t}{n * F * \rho} \tag{5}$$

where I_c is the static corrosion current (A), M is the molar mass (g/mole), t is the total time (s), n is the valence electron concentration of the sample, F is the Faraday constant, and ρ is the density of the sample (g/mm^3).

The friction-promoted corrosion volume loss ($V_{f\text{-}c}$) can likewise be derived from the above equation, where the corrosion current $I_{f\text{-}c}$ is characterized by:

$$I_{f-c} = I_f - I_c \tag{6}$$

where I_f and I_c are the corrosion currents during sliding and static conditions, respectively. The corrosion-promoted friction volume loss ($V_{c\text{-}f}$) can be obtained from the difference between the total volume loss and other volume losses. Based on this framework, the proportional contributions of individual volume loss components for ClS, ClBrS, and BrS during sliding under polarization were quantitatively determined, as summarized in Fig. 10. The total material loss (V_t) of ClS was undoubtedly the highest and not reiterated here. Its synergistic components ($V_{c\text{-}f} + V_{f\text{-}c}$) accounted for 84 % of V_t, significantly exceeding those of ClBrS (80 %) and BrS (72 %). This demonstrates that compared to Br^-, Cl^- not only intensifies tribocorrosion damage but also increases the proportional contribution of synergistic mechanisms to overall material loss. In addition, the proportion of $V_{c\text{-}f}$ was much higher than that of $V_{f\text{-}c}$, indicating that corrosion-promoted friction dominated the synergistic interaction.

The following equation was used to further compare the enhancement of corrosion, friction and synergy by Cl^- and Br^- [49,50]:

$$\alpha = \frac{V_c + V_{f-c}}{V_c} \tag{7}$$

$$\beta = \frac{V_f + V_{c-f}}{V_f} \tag{8}$$

$$\gamma = \frac{V_t}{V_f + V_c} \tag{9}$$

where α, β and γ represent the enhancement factors of corrosion, friction and synergy, respectively. The calculation results are shown in Fig. 11.

The α value was the highest for all samples, indicating that sliding significantly accelerated the corrosion of the samples. In addition, the β and γ values were very close, suggesting that the friction enhancement factor can be approximated as equal to the synergy. It was noteworthy that the α, β, and γ values of ClS were consistently higher than those of ClBrS and BrS (particularly α). This means that during the sliding process, Cl^- plays a more significant role than Br^- in enhancing corrosion, friction, and synergy. Briefly, Cl^- causes more severe damage than Br^- during the tribocorrosion process, which is primarily attributed to the synergistic interaction between friction and corrosion amplifying material loss.

3.5. Tribocorrosion mechanism

Based on the above results, the tribocorrosion diagrams of stainless steel in Cl^- and Br^- solutions are shown in Fig. 12. During the corrosion process (Fig. 12a, c), Cl^- exhibits greater aggressiveness towards the Cr_2O_3 passive film compared to Br^-, resulting in the formation of deeper

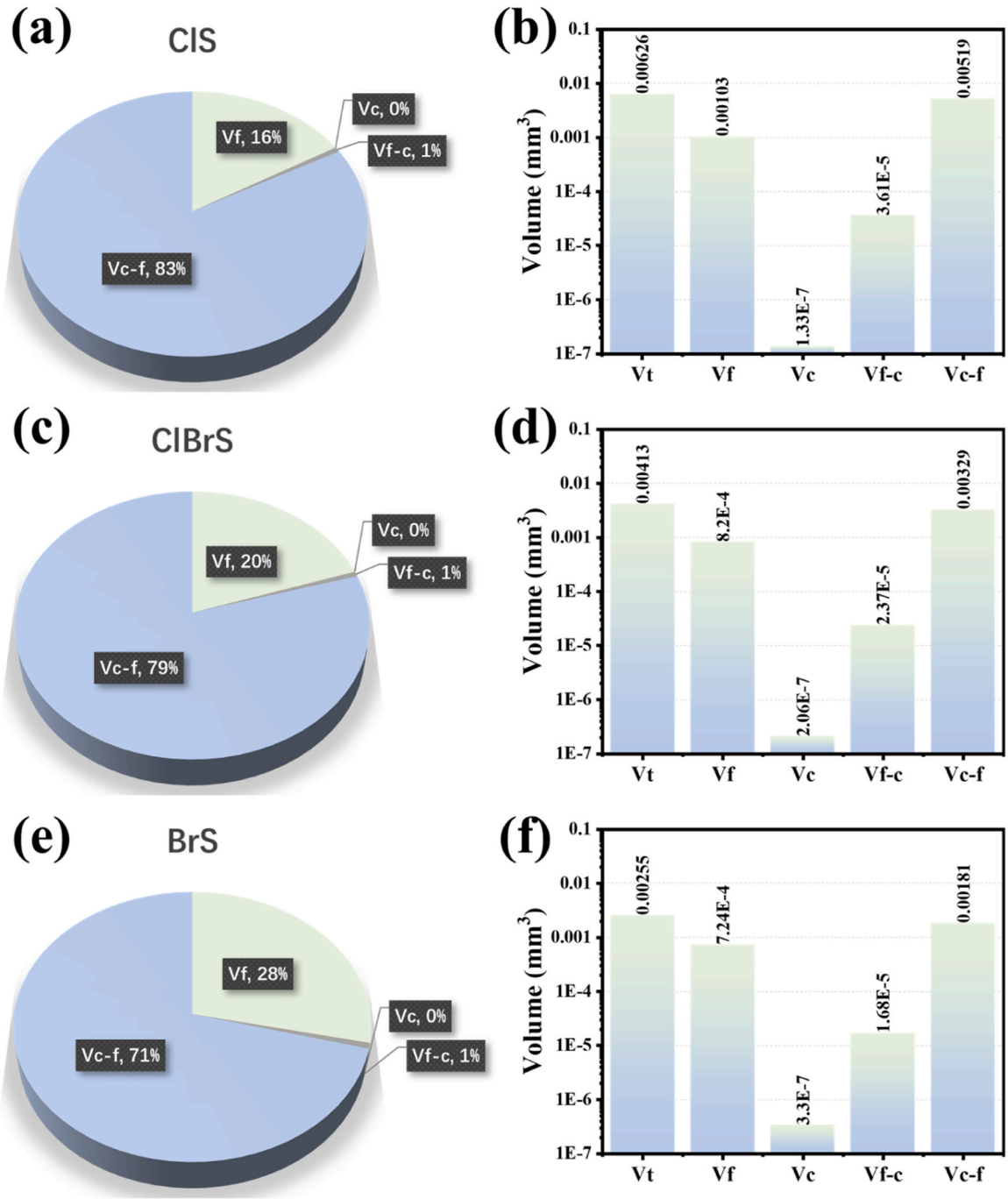

Fig. 10. (a, b) ClS, (c, d) ClBrS, and (e, f) BrS volume loss proportions of individual components during sliding under polarized (dynamic potential) conditions.

and wider pits on the stainless steel surface. However, the severe corrosion damage leads to the accumulation of substantial Fe_xO_y products around the pits, which subsequently inhibit the further penetration of aggressive Cl^- ions. Consequently, a lower I_{corr} is observed for stainless steel in the Cl^- solution compared to the Br^- solution.

Unfortunately, during the tribocorrosion process (Fig. 12b, d), the substantial amount of corrosion products formed on the stainless steel in the Cl^- solution acts as hard third bodies, resulting in severe abrasive wear and exacerbated material loss. Moreover, the large area of freshly exposed surface becomes more susceptible to attack by Cl^- ions, further accelerating the material corrosion damage. In short, Cl^- induces more severe localized corrosion in stainless steel compared to Br^-. The accumulated corrosion products can form a protective barrier, achieving a "rust barrier effect" that mitigates further corrosion. However, under dynamic tribocorrosion, these otherwise protective products act as hard abrasive particles, significantly exacerbating the tribocorrosion damage of the stainless steel.

In pure corrosion processes (particularly under potentiostatic conditions), the material exhibits a relatively broad and stable passive region, where the steady-state current density aligns well with the High Field Model (HFM) [51]. This suggests that the initial growth stage of the passive film is controlled by ion migration under a high electric field. However, HFM fails to explain the transient current peaks and rapid recovery kinetics observed under tribocorrosion conditions, as it does not account for the generation and transport of point defects. In contrast, the Point Defect Model (PDM) provides a more comprehensive interpretation [52,53]. During tribocorrosion, mechanical wear instantly removes the surface passive film. According to the PDM, the freshly

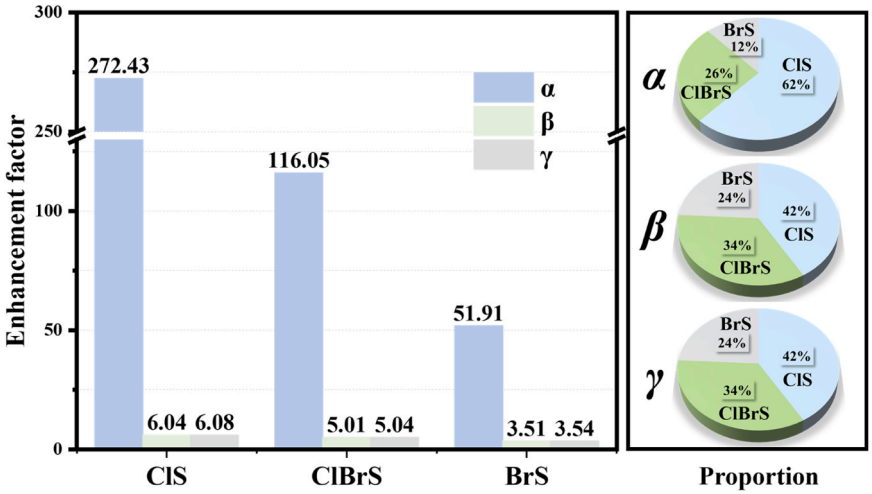

Fig. 11. Corrosion, friction, and synergy enhancement factors of ClS, ClBrS, and BrS.

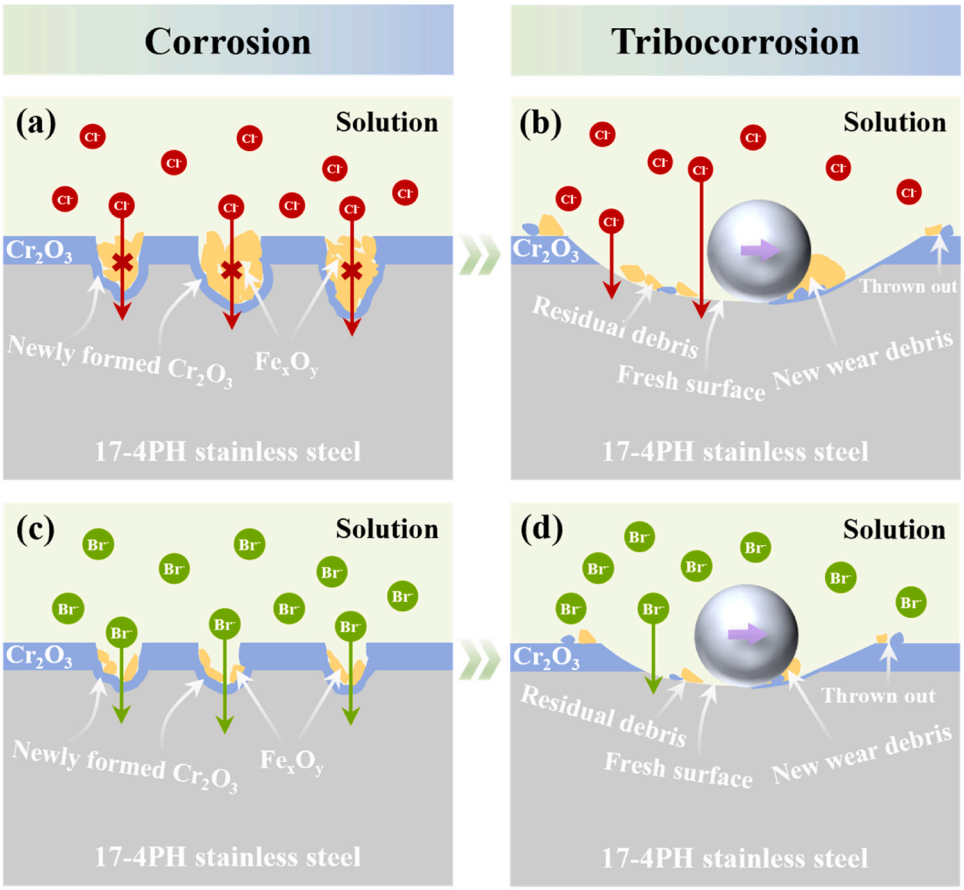

Fig. 12. Schematic diagrams of the tribocorrosion processes of (a, b) ClS and (c, d) BrS.

exposed metal surface triggers intense generation of point defects (such as cation vacancies) at the metal/film interface. The rapid migration and annihilation of these defects drive the repassivation process, corresponding to the quick current decay following the peak. Furthermore, the PDM mechanism, where point defects accumulate at interfaces and cause localized breakdown, offers a good analogy to the continuous localized damage induced by mechanical wear. This explains why the total material loss under tribocorrosion is significantly greater than the simple sum of pure wear and pure corrosion losses, indicating a strong synergistic effect. Therefore, the PDM better represents the processes observed in this study. While HFM can describe the formation of static passive films, only the PDM reasonably explains the core mechanism of dynamic film damage and reformation under mechanical disturbance, providing deeper insight into the nature of tribocorrosion.

4. Conclusion

In summary, a systematic comparative study was conducted on the corrosion and tribocorrosion behavior of 17–4PH stainless steel in Cl^- and Br^- solutions. The results demonstrate that under static corrosion

conditions, the activation energy barrier for the rate-determining step (RDS) of Cl^- (0.16 eV) is significantly lower than that of Br^- (1.42 eV), indicating a stronger capability of Cl^- to displace oxygen in the Cr_2O_3 passive film. Furthermore, Cl^- exhibits superior penetration ability due to its smaller ionic radius. Consequently, stainless steel is more susceptible to pitting corrosion in Cl^- solutions, where larger and denser corrosion pits are observed. However, the accumulation of corrosion products such as Fe_xO_y can hinder the penetration of Cl^-. Consequently, compared to the Br^- solution (8.87×10^{-9} A/cm^2), the stainless steel exhibited a lower I_{corr} in the Cl^- solution (3.58×10^{-9} A/cm^2), demonstrating an inhibitory effect of corrosion products on further corrosion. Under dynamic tribocorrosion conditions, the abundant corrosion products in the Cl^- solution act as third-body abrasives, inducing more severe abrasive wear in stainless steel compared to the Br^- solution. Moreover, the freshly exposed active surfaces further accelerate corrosion. This synergistic interaction between wear and corrosion substantially accelerates material degradation. Additionally, within this synergy, the enhancement coefficients for both corrosion and wear in Cl^- (272.43, 6.04) significantly exceed those in Br^- (51.91, 3.51).

In halide environments such as marine and chemical industries containing Cl^- and Br^-, the passive film on stainless steel is more susceptible to attack by Cl^-, leading to severe corrosion damage. Under static conditions, corrosion products (e.g., Cr_2O_3, Fe_xO_y) form a protective layer that effectively inhibits further corrosion, achieving a "rusting to prevent rust" effect. However, under dynamic tribocorrosion conditions, the synergistic interaction between corrosion and wear transforms these protective corrosion products into primary contributors to accelerated wear. Consequently, particular attention should be paid to the degradation of stainless steel in Cl^- environments, especially under dynamic conditions involving mechanical/tribological interactions. This work not only elucidates the corrosion and tribocorrosion mechanisms of stainless steel in halide solutions (Cl^-/Br^-), but also provides fundamental insights for developing protective strategies in corrosive service environments. In follow-up studies, experiments involving different testing conditions (e.g., contact stress, frequency) and passive substrates/coatings (such as titanium alloys, cermets) may lead to interesting new findings.

CRediT authorship contribution statement

Zheng Wang: Methodology, Investigation. **Yalan Zhang:** Writing – review & editing, Software. **Lei Li:** Formal analysis, Data curation. **Peng Guo:** Methodology. **Aiying Wang:** Writing – review & editing, Supervision, Funding acquisition. **Yingpeng Zhang:** Writing – original draft, Investigation, Data curation.

Declaration of Competing Interest

The authors declare that they have no known competing financial interests or personal relationships that could have appeared to influence the work reported in this paper.

Acknowledgments

This work was financially supported by the National Natural Science Foundation of China (52471146), Specialty Fund of Zhejiang Institute of Tianjin University (Grant No. ZITJU2024-ZYHT006), and Start-up Fund from Ningbo University of Technology (2130011540034).

Appendix A. Supporting information

Supplementary data associated with this article can be found in the online version at doi:10.1016/j.corsci.2026.113643.

Data availability

The raw/processed data required to reproduce these findings cannot be shared at this time as the data also forms part of an ongoing study.

References

[1] Y. Xiong, J. Radhakrishnan, S. Huang, Y. Chua, W. Shi, U. Ramamurty, Corrosion and stress corrosion cracking resistances of the 17-4 precipitation hardened martensitic stainless steel additively manufactured using binder jet printing, Acta Mater. 281 (2024) 120417.
[2] Y. Xia, D. Zhou, W. Qin, Z. Gao, C. Lv, W. Hu, The synergistic effect of microstructure evolution on corrosion resistance-mechanical properties of carbon steel/stainless steel cladding tubes during heat treatment, Corros. Sci. (2025) 113185.
[3] H. Liu, J. Chen, X. Tian, Z. Wang, Y. Zhang, Y. Yan, Effect of fretting regimes on the fretting corrosion behavior of stainless steel in artificial crevices, Corros. Sci. 231 (2024) 111984.
[4] L. Zhao, X. Chen, W. Chang, Q. Liu, H. Qian, D. Guo, C.T. Kwok, L.M. Tam, D. Zhang, Effect of microstructure evolution on microbiologically influenced corrosion of friction stir welded 17-4PH stainless steel, Corros. Sci. (2025) 112977.
[5] D.-I. Seo, J.-B. Lee, Effects of competitive anion adsorption (Br− or Cl−) and semiconducting properties of the passive films on the corrosion behavior of the additively manufactured Ti–6Al–4V alloys, Corros. Sci. 173 (2020) 108789.
[6] S. Zhang, Y. Wang, S. Li, Z. Wang, H. Chen, L. Yi, X. Chen, Q. Yang, W. Xu, A. Wang, Concerning the stability of seawater electrolysis: a corrosion mechanism study of halide on Ni-based anode, Nat. Commun. 14 (2023) 4822.
[7] R. Guo, M. Ives, Pitting susceptibility of stainless steels in bromide solutions at elevated temperatures, Corrosion 46 (1990) 125–129.
[8] L. Lei, Y. Sun, K. Zheng, X. Wang, P. He, Y. Liu, Q. Yao, L. Yin, Y. Wan, J. Li, A comparative study on the critical pitting criteria of a super ferritic stainless steel at different temperatures in chloride or bromide solution, Corros. Sci. 183 (2021) 109311.
[9] J.A. Bardwell, B. MacDougall, Involvement of surface oxide films on iron in halide-induced pitting, Electrochim. Acta 34 (1989) 229–232.
[10] Z. Shao, D. Yu, D. Shao, Y. Du, D. Zheng, Z. Qiu, B. Wu, A protective role of Cl− ion in corrosion of stainless steel, Corros. Sci. 226 (2024) 111631.
[11] M. Kimura, M. Kaneko, N. Ohta, In situ analysis of pitting corrosion in artificial crevice of stainless steel by X-ray absorption fine structure, ISIJ Int. 42 (2002) 1399–1403.
[12] M. Kaneko, H. Isaacs, Effects of molybdenum on the pitting of ferritic-and austenitic-stainless steels in bromide and chloride solutions, Corros. Sci. 44 (2002) 1825–1834.
[13] R.J. Wood, Marine wear and tribocorrosion, Wear 376 (2017) 893–910.
[14] Y. Wang, C. Hu, Y. Wang, H. Fang, J. Li, J. Yu, Tribocorrosion behaviors of WC-10Co-4Cr, WC-20Cr3C2-7Ni, and Cr3C2-25NiCr cermet coatings fabricated by HVAF thermal spraying, Tribol. Int. (2025) 110900.
[15] K. Wang, Z. Zhang, R.S.B. Dandu, W. Cai, Understanding tribocorrosion of aluminum at the crystal level, Acta Mater. 245 (2023) 118639.
[16] M.De Stefano, A. Ruggiero, Tribocorrosion of couplings in seawater environment: an investigation on the positive-negative role of synergy, Tribol. Int. 200 (2024) 110143.
[17] R.J. Wood, S. Herd, M.R. Thakare, A critical review of the tribocorrosion of cemented and thermal sprayed tungsten carbide, Tribol. Int. 119 (2018) 491–509.
[18] A. Barroux, N. Ducommun, E. Nivet, L. Laffont, C. Blanc, Pitting corrosion of 17-4PH stainless steel manufactured by laser beam melting, Corros. Sci. 169 (2020) 108594.
[19] H. Ma, R. Liu, P. Ke, Y. Cui, L. Liu, F. Wang, Effect of hydrostatic pressure on the pitting corrosion of 17-4PH martensitic stainless steel, Eng. Fail. Anal. 138 (2022) 106367.
[20] A. Ruggiero, M.De Stefano, Experimental investigation on the bio-tribocorrosive behavior of Ti6Al4V alloy and 316 L stainless steel in two biological solutions, Tribology Int. 190 (2023) 109033.
[21] K. Ujihara, M. Nishimoto, I. Muto, Microelectrochemical identification of the submicron-sized initiation site for pitting corrosion in 17–4PH stainless steel, Corros. Sci. 251 (2025) 112939.
[22] D. Guo, J. Chen, X. Chen, Q. Shi, V. Cristino, C. Kwok, L. Tam, H. Qian, D. Zhang, X. Li, Pitting corrosion behavior of friction-surfaced 17-4PH stainless steel coatings with and without subsequent heat treatment, Corros. Sci. 193 (2021) 109887.
[23] M.De Stefano, S.M. Aliberti, A. Ruggiero, Bio) Tribocorrosion in dental implants: principles and techniques of investigation, Appl. Sci. 12 (2022) 7421.
[24] Y. Zhang, Q. Wang, G. Chen, C.S. Ramachandran, Mechanical, tribological and corrosion physiognomies of CNT-Al metal matrix composite (MMC) coatings deposited by cold gas dynamic spray (CGDS) process, Surf. Coat. Technol. 403 (2020) 126380.
[25] A. Ruggiero, M.De Stefano, The effect of chemical composition of biological solutions on the tribocorrosive behavior and synergistic wear of Titanium grade V alloys for biomedical applications, J. Bio TriboCorros. 10 (2024) 63.
[26] X. Zhou, Y. Zhang, P. Guo, L. Cui, A. Wang, P. Ke, Tribological behavior of Cr/aC multilayered coating against PEEK under dry sliding condition, Wear 518 (2023) 204625.
[27] G. Kresse, J. Furthmüller, Efficient iterative schemes for ab initio total-energy calculations using a plane-wave basis set, Phys. Rev. B 54 (1996) 11169.

[28] G. Kresse, J. Hafner, Ab initio molecular-dynamics simulation of the liquid-metal–amorphous-semiconductor transition in germanium, Phys. Rev. B 49 (1994) 14251.
[29] J.P. Perdew, K. Burke, M. Ernzerhof, Generalized gradient approximation made simple, Phys. Rev. Lett. 77 (1996) 3865.
[30] Y. Liu, S. Li, H. Li, G. Ma, L. Sun, P. Guo, P. Ke, K.-R. Lee, A. Wang, Controllable defect engineering to enhance the corrosion resistance of Cr/GLC multilayered coating for deep-sea applications, Corros. Sci. 199 (2022) 110175.
[31] Y. Zhang, H. Li, L. Cui, W. Yang, G. Ma, R. Chen, P. Guo, P. Ke, A. Wang, Comparative study on tribocorrosion behavior of hydrogenated/hydrogen-free amorphous carbon coated WC-based cermet in 3.5 wt% NaCl solution, Corros. Sci. 227 (2024) 111738.
[32] N. Hakiki, M. Montemor, M. Ferreira, M. da Cunha Belo, Semiconducting properties of thermally grown oxide films on AISI 304 stainless steel, Corros. Sci. 42 (2000) 687–702.
[33] M. Carmezim, A. Simoes, M. Montemor, M.D.C. Belo, Capacitance behaviour of passive films on ferritic and austenitic stainless steel, Corros. Sci. 47 (2005) 581–591.
[34] T. Hoar, D. Mears, G. Rothwell, The relationships between anodic passivity, brightening and pitting, Corros. Sci. 5 (1965) 279–289.
[35] J. Soltis, Passivity breakdown, pit initiation and propagation of pits in metallic materials–review, Corros. Sci. 90 (2015) 5–22.
[36] P. Marcus, V. Maurice, H.-H. Strehblow, Localized corrosion (pitting): a model of passivity breakdown including the role of the oxide layer nanostructure, Corros. Sci. 50 (2008) 2698–2704.
[37] T. Hoar, The production and breakdown of the passivity of metals, Corros. Sci. 7 (1967) 341–355.
[38] W. Wang, K. Wang, Z. Zhang, J. Chen, T. Mou, F.M. Michel, H. Xin, W. Cai, Ultrahigh tribocorrosion resistance of metals enabled by nano-layering, Acta Mater. 206 (2021) 116609.
[39] Z. Wang, Y. Yan, Y. Wu, X. Huang, Y. Zhang, Y. Su, L. Qiao, Corrosion and tribocorrosion behavior of equiatomic refractory medium entropy TiZr (Hf, Ta, Nb) alloys in chloride solutions, Corros. Sci. 199 (2022) 110166.
[40] Y. Liu, L. Liu, S. Li, R. Wang, P. Guo, A. Wang, P. Ke, Accelerated deterioration mechanism of 316L stainless steel in NaCl solution under the intermittent tribocorrosion process, J. Mater. Sci. Technol. 121 (2022) 67–79.
[41] L. Zhao, H. Qian, W. Chang, D. Guo, C.T. Kwok, L.M. Tam, D. Zhang, Effect of aging heat treatment on microbiologically influenced corrosion of 17–4PH stainless steel by Pseudomonas aeruginosa, Corros. Sci. 227 (2024) 111739.
[42] A. Barroux, T. Duguet, N. Ducommun, E. Nivet, J. Delgado, L. Laffont, C. Blanc, Combined XPS/TEM study of the chemical composition and structure of the passive film formed on additive manufactured 17-4PH stainless steel, Surf. Interfaces 22 (2021) 100874.
[43] X. Huang, D. Costa, B. Diawara, V. Maurice, P. Marcus, DFT study on Mo-stabilized passive films: hydroxylation effects on chromium and iron oxide surfaces, Corros. Sci. 233 (2024) 112105.
[44] B. Lynch, Z. Wang, L. Ma, E.-M. Paschalidou, F. Wiame, V. Maurice, P. Marcus, Passivation-induced Cr and Mo enrichments of 316L stainless steel surfaces and effects of controlled pre-oxidation, J. Electrochem. Soc. 167 (2020) 141509.
[45] A. Brooks, C. Clayton, K. Doss, Y. Lu, On the role of Cr in the passivity of stainless steel, J. Electrochem. Soc. 133 (1986) 2459.
[46] E. Gardin, S. Zanna, A. Seyeux, A. Allion-Maurer, P. Marcus, Comparative study of the surface oxide films on lean duplex and corresponding single phase stainless steels by XPS and ToF-SIMS, Corros. Sci. 143 (2018) 403–413.
[47] F. Mansfeld, B. Little, A technical review of electrochemical techniques applied to microbiologically influenced corrosion, Corros. Sci. 32 (1991) 247–272.
[48] Y. Zhong, Y. Zhang, C.S. Ramachandran, Q. Wang, Study on tribocorrosion properties of cold spray additively manufactured 2024 Al alloy, Corros. Sci. 233 (2024) 112109.
[49] J. Wang, W. Wen, J. Cheng, L. Dai, S. Li, X. Zhang, Y. Yang, H. Li, X. Hou, B. Wu, Tribocorrosion behavior of high-entropy alloys FeCrNiCoM (M= Al, Mo) in artificial seawater, Corros. Sci. 218 (2023) 111165.
[50] H. Mraied, W. Cai, The effects of Mn concentration on the tribocorrosion resistance of Al–Mn alloys, Wear 380 (2017) 191–202.
[51] L. Zhang, D.D. Macdonald, E. Sikora, J. Sikora, On the kinetics of growth of anodic oxide films, J. Electrochem. Soc. 145 (1998) 898.
[52] D.D. Macdonald, E. Sikora, J. Sikora, The kinetics of growth of the passive film on tungsten in acidic phosphate solutions, Electrochim. Acta 43 (1998) 2851–2861.
[53] G.R. Engelhardt, D. Chen, C. Dong, D.D. Macdonald, Estimation of some parameters in the point defect model (PDM) for the passivity of metals, J. Electrochem. Soc. 171 (2024) 031503.